

Columnar Disorder and Low-temperature Properties of the Intermetallic Kagomé $MgCo_6Ge_6$

Mekhola Sinha,^{1,2} Hector K. Vivanco,^{1,2} Cheng Wan,^{1,2} Maxime A. Siegler,¹ Veronica J. Stewart,^{1,2} Lucas A. Pressley,^{1,2} Tanya Berry^{1,2}, Ziqian Wang,³ Isaac Johnson,³ Mingwei Chen,^{3,4} Thao T. Tran^{1,2,†}, W. Adam Phelan,^{1,2,‡} and Tyrel M. McQueen*^{1,2,3}

¹ Department of Chemistry, The Johns Hopkins University, Baltimore, Maryland 21218, USA

² Institute for Quantum Matter, Department of Physics and Astronomy, The Johns Hopkins University, Baltimore, Maryland 21218, USA

³ Department of Materials Science and Engineering, The Johns Hopkins University, Baltimore, MD 21218, USA

⁴ WPI Advanced Institute for Materials Research, Tohoku University, Sendai 980-8577, Japan

*Present Address: Department of Chemistry, Clemson University, Clemson, SC 29634, USA

†Present Address: Los Alamos National Laboratory, New Mexico 87544, USA

ABSTRACT: Layered intermetallic compounds with kagomé lattices provide access to the electronic structures and exotic phenomena associated with flat bands and Dirac-type dispersion that are enforced by atomic connectivity. Here, we report the preparation of $\sim 20\text{mm} \times 5\text{mm}$ single crystals of $MgCo_6Ge_6$ via laser Bridgman growth. X-ray precession images and electron diffraction measurements show $MgCo_6Ge_6$ crystallizes in space group $P6/mmm$, with $a = 5.06094(15)$ Å, $c = 7.7271(2)$ Å. The structure, solved at $T = 293(2)$ K, consists of eclipsed Co kagomé and hexagonal Ge layers with Mg and (Ge_2) dimers filling the hexagonal channels. Residual electron density maps provide evidence of Ge-Ge disorder along the c axis. Magnetization measurements indicate Pauli paramagnetic behavior with a crystalline anisotropy developing below $T \sim 20$ K. Resistivity data show a metallic temperature dependence, with evidence of an electron-electron scattering driven contribution of $A = 58(13) \times 10^{-5}$ mΩ.cm.K². Specific heat measurements show a low temperature electronic contribution of $\gamma = 20.84(28)$ mJ.K².mol⁻¹. The Kadowaki-Woods ratio is $0.134(21) \times 10^{-2}$ μΩ.cm.mol².K².mJ⁻², comparable to hexagonal layered $Na_{0.7}CoO_2$ and strongly enhanced Wilson ratio of $\sim 7.7 - 5.2$ similar to strongly correlated layered cobalt oxide $[BiBa_{0.66}K_{0.36}O_2]CoO_2$. Analysis of the phonon density of states extracted from specific heat shows the existence of a low-lying Einstein-like contribution ($T_{op} = 121.41(47)$ K), a feature absent in the related compounds YCr_6Ge_6 and $LuFe_6Ge_6$. Our results add to the knowledge of kagomé metals and suggest directions for future exploration to connect structural and electronic behaviors in these fascinating materials.

I. INTRODUCTION

Crystalline materials containing the kagomé lattice are attracting considerable attention in the field of quantum physics. The unique 2D triangular network of metal ions serves as an exciting route for theoretical modelling as well as experimental realization of novel quantum phases. The kagomé lattice combined with lattice symmetry, unusual magnetism and spin orbit coupling makes these materials a perfect host for novel topological phenomena [1-5]. The lattice geometry favors the complete destructive interference of electronic wave functions by nearest neighbor interactions creating

potential non-dispersive strongly correlated flat bands in momentum space [6,7], but it houses symmetry protected Dirac bands similar to graphene [8,9]. Despite this family of compounds being in the spotlight due to theoretical predictions, experimental realization of an idealized 2D kagomé lattice in bulk crystals is challenging. In terms of binary intermetallic kagomés, Fe_3Sn_2 [10-12] and $CoSn$ [6,13] are the only compounds where quasi-2D electronic structure has been detected. The most studied metallic ternary compounds are $Co_3Sn_2S_2$ [14-16], with 3D magnetic Weyl points as the potential source of chiral anomaly

in transport, and $TbMn_6Sn_6$, a topological kagomé magnet candidate [17]. The recent observation of highly dispersive Dirac bands by angle-resolved photoelectron spectroscopy (ARPES) has led to the discovery of giant extrinsic Anomalous Hall Effect (AHE) in metallic KV_3Sb_5 [18,19].

The family of compounds with the general formula MT_6X_6 (M = Li, Mg, Zr, Hf, rare-earth elements; T = Cr, Mn, Fe, Co, Ni; X = Si, Ge, Sn) generally crystallize in the $HfFe_6Ge_6$ structure ($P6/mmm$) [19-21]. The crystal structure of MT_6X_6 (X = Ge) contains alternating planar graphene-type layers of Ge and 2D T kagomé nets along the crystallographic c axis. The resulting columns of vertex sharing bipyramids form a 3D T-Ge honeycomb lattice with M and Ge atoms occupying the interstitial sites. We focus on a specific type of MT_6X_6 compounds with X = Ge, which has garnered attention with reports of structural disorder [22] and unusual physical properties owing to the presence of flat bands near the Fermi level [23,24]. Despite the atomic structure playing a key role in governing the electronic structure and physical properties of these compounds there has been no single crystal studies exploring the connection between the underlying structure and reported physics.

Here we report the growth of single crystals of $MgCo_6Ge_6$. Growing crystals of Mg compounds containing transition metals means dealing with the high vapor pressure of the first and the high melting temperature of the latter. Often the flux method is used to obtain single crystals. By using a flux it is possible to solve the high melting issue by obtaining a melt at lower temperatures with moderate vapor pressures that is suitable for the growth [25,26]. In some cases, the use of a solvent leads to the formation of unwanted phases; in such cases, self-flux can be useful [27]. Such fluxes can also be used as traveling solvents in a floating zone, Bridgman, or laser pedestal geometry to grow larger samples. Even using a flux or traveling solvent, growth temperatures might exceed $T \sim 1200$ °C which makes it harder to control the vapor pressure and almost impossible to control the decomposition of intermetallics. The vaporization can be controlled by applying inert gas pressure during the growth. Furthermore, the heating source plays an important role in the growth. The precision of laser heating enables stabilization [28] of a uniform, but small, molten volume in a

Bridgman growth geometry, thus minimizing the vaporization of Mg. We look into correlating the single crystal structure observed from solution to Single Crystal X-Ray Diffraction (SXRD) data with the low temperature phonon modes obtained from fitting heat capacity data. Magnetic and resistivity measurements done on the single crystals reveal low temperature magnetic anisotropy and Kadowaki-Woods ratio comparable to hexagonal layered compound $Na_{0.7}CoO_2$. The Wilson ratio is enhanced similar to strongly correlated layered cobalt oxides. Further study the band structure of similar systems to gain insight on future directions to correlate the structural and electronic properties.

II. EXPERIMENTAL SECTION

A. Synthesis

Stoichiometric amounts of germanium (Alfa Aesar, 99.97%), cobalt (Alfa Aesar, 99.7%) and magnesium (Alfa Aesar, 99%) were mixed in a molar ratio of 1:6:12 and heated at 120 °C/hr to 850 °C, held for 12 h, and then cooled to room temperature at 120 °C/hr, all in a 95% Ar, 5% H_2 atmosphere in a tube furnace. The sample was reground and the process was repeated three times. A zirconium foil oxygen getter was placed at the gas inlet of the tube furnace to prevent oxidation from residual H_2O/O_2 in the gas stream. The resulting product was purified by washing with 3 M HCl to remove residual oxide contaminants.

$MgCo_6Ge_6$ crystals were grown by Bridgman technique in a Laser Diode Floating Zone (LDFZ) furnace (Crystal Systems Inc FD-FZ-5-200-VPO-PC) with 5 × 200 W GaAs lasers (976 nm) as the heating source; further details are included in the results section below. Hexagonal plate-like single crystals of YCr_6Ge_6 (~ 2 mm edges) and $LuFe_6Ge_6$ (~ 1 mm edges) were obtained by previously reported flux crystal growth techniques [18,20].

B. Characterization

SXRD data were collected at $T = 293(2)$ K using a SuperNova diffractometer (equipped with an Atlas detector) with Mo- $K\alpha$ radiation ($\lambda = 0.71073$ Å) using the program CrysAlisPro (version 1.171.36.32 Agilent Technologies, 2013). The same program was used to refine the cell dimensions and for data reduction. The

crystal structures were solved in WinGx and refined with the program SHELXS-2008 [21]. Electron diffraction images were collected using a Phillips CM300 atomic resolution Transmission Electron Microscope (TEM) equipped with a Field Emission Gun with an accelerating voltage of 300 kV. The selected area electron diffraction (SAED) patterns were taken from crushed crystals suspended in acetone on a carbon-coated Cu grid. A Quantum Design Physical Properties Measurement System (PPMS) was used for the heat capacity measurements from $T \sim 1.9$ to 300 K at $\mu_0 H = 0$ T using the semi-adiabatic method and a 1% temperature rise. Resistivity was conducted by four-probe method in the PPMS from $T \sim 1.9$ to 300 K at $\mu_0 H = 0$ T and the magnetization measurements were done at $\mu_0 H = 1$ T in the same temperature range. 3D Micro-Computed Tomography (μ CT) data was collected using a Bruker Skyscan 1172 with the X-ray source set to 80 kV/124 μ A. Frames were collected in 0.1° steps over 180° using an Al/Cu filter and a SHT 11 MP camera, averaging 10 frames per step and 3400 ms of exposure per step. 3D reconstruction was performed using NRecon software with smoothing, ring artifact correction, and beam hardening correction applied. Data were visualized using Dragonfly software by ORS.

C. Theory

Density Functional Theory (DFT) calculations were performed with an all-electron full-potential linearized augmented-plane wave basis with local

(Electrons in K-Space)[22]. A $6 \times 6 \times 4$ k-point mesh is used in sampling the Brillouin zone with spin-orbit coupling (SOC) applied. All data were processed using Origin 2020 and structures were visualized using the Vesta software [29].

III. RESULTS AND DISCUSSION

A. Single Crystal Growth

The synthesized powder was compacted into a graphite crucible (typically ~ 6 mm in diameter and ~ 50 mm long). The graphite crucible was moved downwards while the lasers were held at a fixed position (Fig 1a). Only one zone pass was required. Single crystal growth attempts under vacuum or Argon at normal pressure led to decomposition of MgCo_6Ge_6 into Mg and CoGe phases owing to significant vaporization of Mg at the melting temperature. The optimum growth conditions were found to be under 3 bar of dynamic argon gas pressure at $\sim 40\%$ laser power. A high travelling rate of 10 mm/hr and narrow beam cross-section (8x4 mm) of the lasers helped to control the vaporization of Mg and yielded large (around 20 mm in length and 5 mm in diameter) single crystals of MgCo_6Ge_6 . A rotation rate of 10 rpm was used to homogenize the melt and obtain single crystals without observable inclusions. Fig. 1b shows a 3D X-ray Micro Computed Tomography (Micro-CT) slice of an as-grown MgCo_6Ge_6 single crystal grown via the laser Bridgman technique. Micro-CT is a technique suitable for identification of the number, type, and

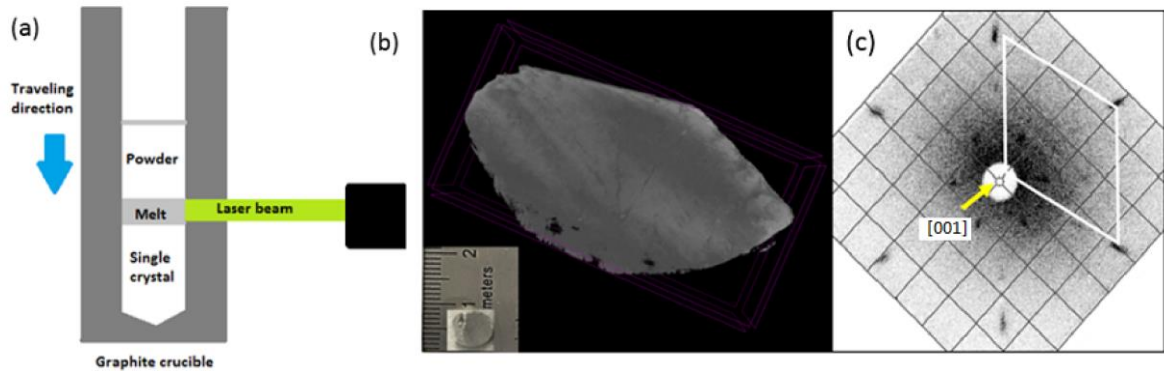


Figure 1. a) The experimental set up for the single crystal growth by Bridgman growth technique using GaAs lasers (only one shown for clarity) as the heating source. (b) X-ray CT scan 3D image showing no inclusions in the obtained single crystal (shown in the inset) in the micrometer range, with dark grey regions near the center being due to beam hardening artifacts. (c) Backscattered X-ray Laue image of a cut crystal taken along [001] direction showing no evidence of twinning.

orbitals (FP-LAPW + LO) as implemented in Elk

distribution of micron-scale inclusions [30], with

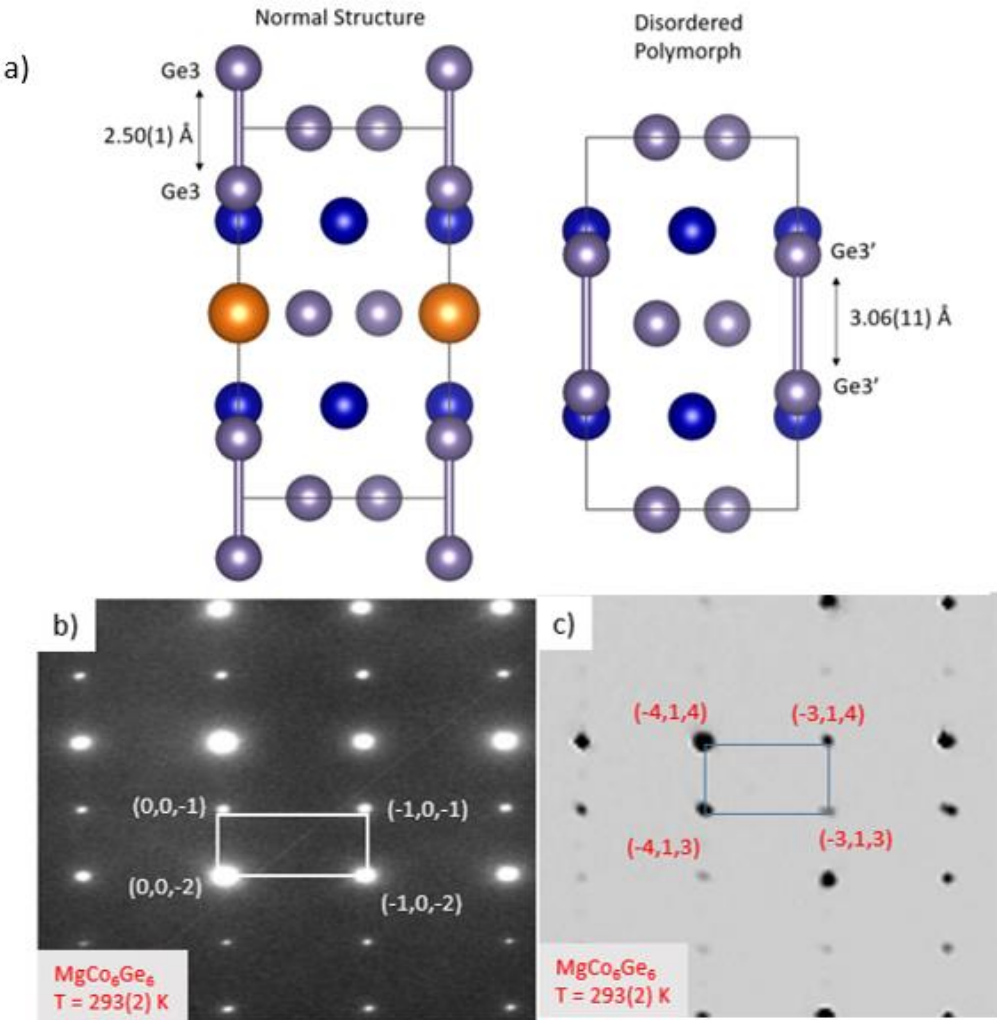


Figure 2. a) The normal and disorder polymorph of the MgCo₆Ge₆ structure along c axis (the grey spheres are Ge atoms, orange sphere are Mg atoms and blue Cobalt) showing the increase in the Ge3'-Ge3' bond distance in the disordered model. b) SAED image of the MgCo₆Ge₆ crystals at T = 293(2) K in the (h0l) and (c) SXRD precession image indexed in P6/mmm in the (h1l) plane for a single crystal at T = 293(2) K. The blue rectangle shows the unit cell reported for P6/mmm peaks which agrees with our SXRD structure solution.

contrast provided by differing attenuation coefficients of secondary phases or crystalline boundaries. Analysis of the 3D scattering volume (SI Video 1) reveals no inclusions in the sample detected up to the limit of the camera resolution and sensitivity. Further, there is an absence of detectable domain boundaries, consistent with a single crystal piece without twinning. Further, a backscattered X-ray Laue diffraction image collected on a piece of cut single crystal along [001] direction shows no evidence of twinning (Fig 1c).

B. Single Crystal Structure: Columnar Disorder

The reported crystal structure of MT₆X₆ (X = Ge) contains alternating planar graphene-type layers of Ge and 2D Co kagomé nets along the crystallographic c axis. The resulting columns of vertex sharing bipyramids form a 3D Co-Ge honeycomb lattice with M and Ge atoms occupying the sites in the 1-D hexagonal channels as shown in Fig. 2 [31]. In agreement with the majority of this structural family, SXRD data (Fig. 2c) suggests a unit cell of P6/mmm with $a = 5.0609(2)$ Å, $c = 7.7271(2)$ Å, also in agreement with electron diffraction data (Fig 2b). Initial attempts to model the T = 293(2) K SXRD data of MgCo₆Ge₆ with the HfFe₆Ge₆ structure resulted in $R_1 = 1.93\%$, $wR_2 = 5.63\%$, $\chi^2 = 1.615$, with anomalously

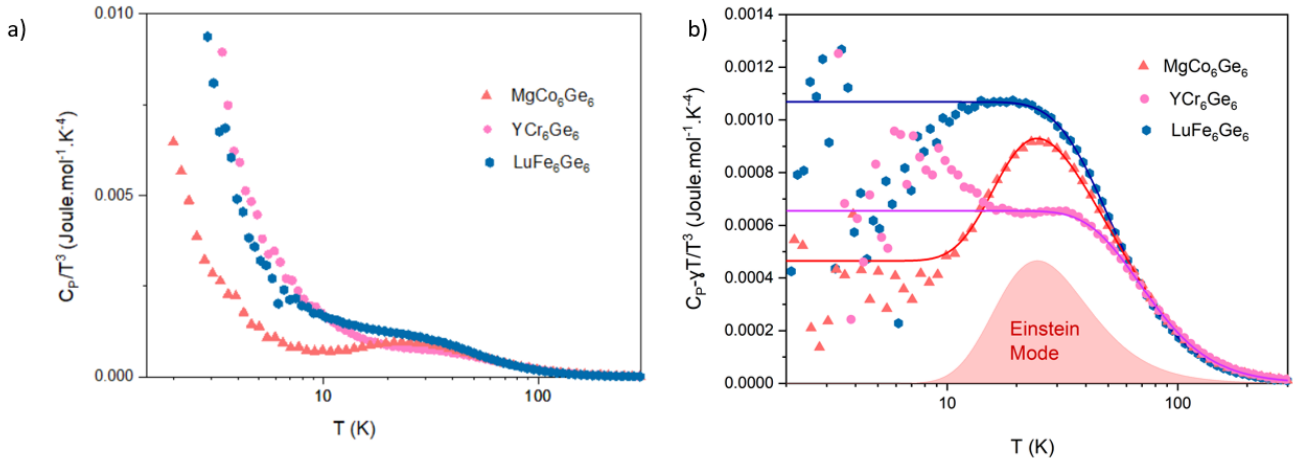


Figure 3. (a) Heat capacity (C_p) divided by temperature cubed (T^3) versus log of temperature (T) for a single crystal piece of $MgCo_6Ge_6$, YCr_6Ge_6 and $LuFe_6Ge_6$. (b) C_p/T^3 versus log of T plot after the subtraction of the electronic contribution ($y.T$) from C_p to approximate the one-dimensional phonon density of states. The solid lines show fits to the experimental data. The most noticeable difference between the fits is the contribution from the low-lying Einstein peak in the $MgCo_6Ge_6$ single crystal which is absent in the other two. This suggests possible presence of disorder or vibrationally active local modes in the structure.

Table I: Characteristic temperatures and number of oscillators of phonon modes obtained from the fit to the specific heat for single crystals of $MgCo_6Ge_6$, YCr_6Ge_6 and $LuFe_6Ge_6$.

$MgCo_6Ge_6$			YCr_6Ge_6			$LuFe_6Ge_6$		
Mode	T (K)	Oscillator Strength (per formula unit)	Mode	T (K)	Oscillator Strength (per formula unit)	Mode	T (K)	Oscillator Strength (per formula unit)
Einstein	121.41(47)	1.56(2)				Debye 1	673(29)	4.97(12)
Debye	363(1)	11.44(2)	Debye	336(1)	12.85(13)	Debye 2	246.89(95)	8.83(12)

large residual electron density in between Mg and Ge3 atoms along c axis). Similar anomalous scattering was observed in neutron powder diffraction studies on $TbCr_6Ge_6$, and interpreted as a partially disordered variant of hexagonal $HfFe_6Ge_6$ structure type ($P6/mmm$) where the Tb -(Ge2)- Tb -(Ge2) chains are shifted by half a unit cell along the c axis [22, 32]. Such disorder would explain the observed excess density in the $MgCo_6Ge_6$; quantitative attempts at refinement gave $R_1 = 1.46\%$, $wR_2 = 4.16\%$, $\chi^2 = 1.163$, but with negative scattering holes in the positions of the displaced Mg ions; removing the Mg ions gave an improved fit to the data, $R_1 = 1.31\%$, $wR_2 = 3.47\%$, $\chi^2 = 1.262$, with a refined fraction of the translated fraction of $\sim 5\%$. We thus conclude that $\sim 5\%$ Mg vacancies, expected on thermodynamic grounds given the volatility of Mg, generate columnar disorder in $MgCo_6Ge_6$ by introducing localized changes in the Ge3-Ge3 stacking along c axis. The covalent bond distance between the Ge3-Ge3 atoms in the majority component is $2.4997(16)$ Å which is considerably shorter than the Ge2-Ge2 distance in

the graphene layers ($2.94(12)$ Å) and indicative of strong Ge-Ge pair formation due to electron donation from the electropositive Mg^{2+} . The disorder accompanied by the absence of Mg^{2+} helps the Ge3'-Ge3' bonds to relax to $3.06(11)$ Å. No such disorder was observed in the single crystals of $LuFe_6Ge_6$ and YCr_6Ge_6 possibly due to less volatility of Lu and Y compared to Mg. This type of disorder is analogous to normal and collapsed structures in planar AB_2X_2 systems. An ideal example in planar AB_2X_2 systems is the pressure-tunable P-P bond distance between $SrRh_2P_2$ (3.284 Å) and $SrPd_2P_2$ (2.217 Å) [33].

C. Low temperature Einstein phonon mode

Both amorphous and crystalline systems have been found to have excess low temperature specific heat than predicted by the Debye model due to low-lying optic phonons, which can arise due to disorder or due to proximity to bond making or breaking or directional rearrangement, such as octahedral tilting in perovskites [34], lone-pair driven disorder in

pyrochlores etc [35]; thus a structure with Ge2 dimers and evidence of disorder may show thermodynamic impacts of those structural components. Fig. 3a shows a plot of C_p/T^3 vs $\log T$; at sufficiently low temperatures Debye modes plateau at a constant value, while Einstein modes account for non-dispersing behaviour [36]. We find a definitive peak that cannot be explained by diffuse vibrational modes at $T \approx 25$ K for MgCo_6Ge_6 . The small feature around $T \approx 3.7$ K is the superconducting transition from the minor amount of leftover Sn flux on the YCr_6Ge_6 crystal. After subtracting the electronic contribution (γ) (Fig 6, discussed later) from the bulk specific heat we try to model the data to reflect the behaviour of the one-dimensional phonon density of states (Fig 3b) [37]. In this model, the Debye (acoustic) contribution is represented by a constant up to θ_D , whereas an Einstein (optical) mode is represented by a peak, resulting from activated low T behaviour. The most striking feature of the plot is a large low temperature peak at $T \approx 25$ K with $\theta_E = 121.41(47)$ K, indicating the data cannot be described by any combination of Debye terms (Table I). The data below $T \approx 10$ K is noisy after the subtraction of the huge electronic contribution from the specific heat. The high energy part of the spectrum in MgCo_6Ge_6 was fit with a Debye contribution having $\theta_D = 363(1)$ K. The θ_D goes down to 336(1) K in YCr_6Ge_6 possibly due to less coupling of the higher mass Y with the Ge atoms compared to Mg. Increases in coupling between the Mg and Ge atoms might result in weakening of the Ge-Ge bonds along c axis in MgCo_6Ge_6 leading to disorder. In the LuFe_6Ge_6 crystal we observe two Debye modes at $\theta_{D1} = 246.89(95)$ K and $\theta_{D2} = 673(29)$ K further confirming the decoupling of the atoms with increasing difference in mass between them. While the low-lying Einstein peak can be described by the vibrations of the local modes, the high temperature Debye mode is associated with higher energy vibrations of atoms having lower masses. Inversely, the lower temperature Debye mode is associated with lower energy vibrations of atoms having higher atomic masses. The total number of oscillators for each of the fits sum to ~ 13 (the number of atoms per formula unit) agreeing well with the theoretical value. No evidence of excess low temperature specific heat associated with local disorder was observed in YCr_6Ge_6 and LuFe_6Ge_6 supporting the origins as columnar disorder tied to Mg vacancies and Ge-Ge bond length changes.

Efforts to fit an Einstein mode in the LuFe_6Ge_6 data resulted in the deviation of the total number of oscillators from ~ 13 . Further, we did not observe any possible phase transitions in any of the single crystals.

D. Low temperature Physical Properties

Temperature dependent magnetic susceptibility ($T \approx 1.8$ to 300 K), estimated as $\chi = M/H$ with an applied field of $\mu_0 H = 1$ T, of a MgCo_6Ge_6 crystal [001] were measured in parallel ($\chi_{//}$) and perpendicular (χ_{\perp}), which are approximately identical at room temperature (Fig. 4). Initial analysis was performed using the Curie-Weiss law. The Curie constant provided by the analysis is 0.006 $\text{emu}\cdot\text{K}\cdot\text{mol}^{-1}\cdot\text{Oe}^{-1}$ for the parallel measurement, where the expected values are 0.37 or 1.87 for a $S = 1/2$ or $S = 3/2$ system, respectively. This analysis indicates that the observed behavior most likely results from impurity spins from surface oxides due to the small magnetic moment. Delocalized electrons can also contribute to magnetic susceptibility as a response to the magnetic field, resulting from Pauli paramagnetism which is indicative of metallic behavior. Furthermore, χ_{\perp} has a different dependence with $\chi_{//}$ below $T \sim 20$ K and χ_{\perp} is about 60% smaller than $\chi_{//}$ as $T \rightarrow 0$ K (Fig. 4 inset). An additional Curie term from a magnetic impurity,

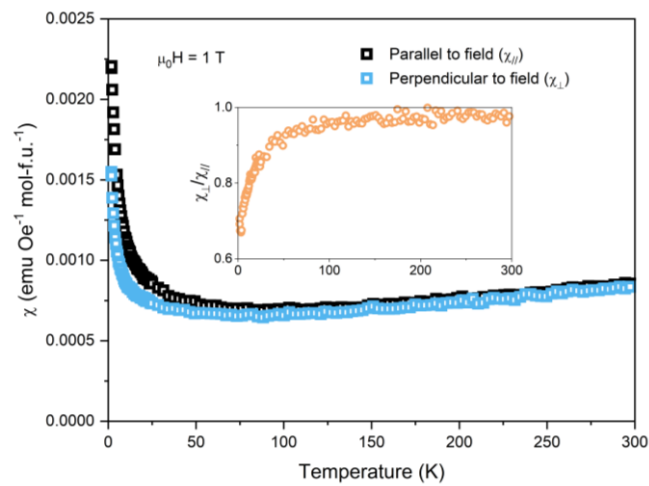


Figure 4. Magnetic susceptibility measured at $\mu_0 H = 1$ T for single crystal MgCo_6Ge_6 . The inset displays the magnetic susceptibility of the crystal [001] oriented perpendicular to the field (χ_{\perp}) over parallel to the field ($\chi_{//}$) demonstrating the anisotropic behavior of MgCo_6Ge_6 . The compound behaves as a paramagnet with low temperature anisotropy observed below $T \sim 20$ K.

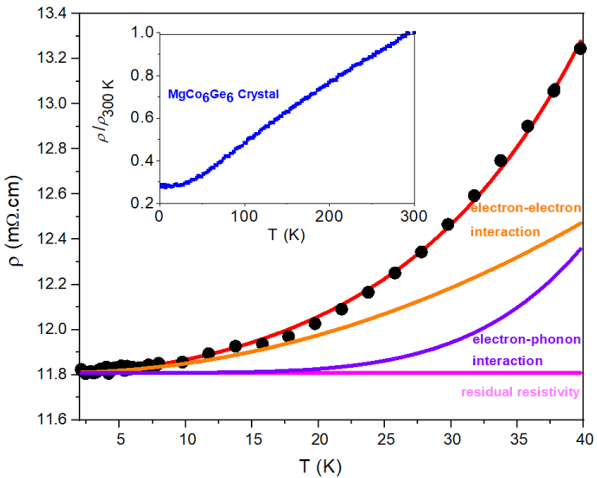


Figure 5. Resistivity measured at $\mu_0H = 0$ T for single crystal MgCo_6Ge_6 [001] (inset) shows no evidence of phase transition between $T \sim 1.8$ K and 300 K. The low temperature region from $T \sim 1.8$ K and 40 K has been fit to the equation $\rho = \rho_0 + AT^2 + BT^5$ where $\rho_0 = 11.808(2)$ mΩ.cm is the residual resistivity, $A = 6(1)*10^{-5}$ mΩ.cm.K² and $B = 5(3) * 10^{-10}$ mΩ.cm.K⁵ are the electron-electron and electron-phonon scattering terms respectively.

which is often observed in spin systems, should be isotropic and cannot explain the anisotropic behavior. Similar behavior has been reported in other similar 2D systems, such as YCr_6Ge_6 and LuFe_6Ge_6 single crystals, although its origin is not clear [9,18]. No evidence of magnetic phase transition was observed down to $T \sim 1.8$ K.

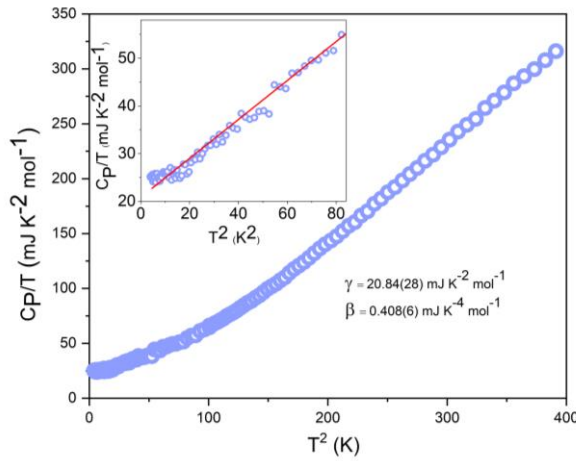


Figure 6. a) Heat Capacity (C_p) divided by T^2 plot of a MgCo_6Ge_6 single crystal piece to extract the experimental Sommerfield coefficient (Y) and β values using the equation $C_p/T = Y + \beta T^2$ using the fit (red line) in the inset.

This observation is consistent with the resistivity measurements shown in Fig 5 (inset) with MgCo_6Ge_6 showing metallic behavior with no anomalies. In the low temperature region below $T \sim 15$ K electron-electron scattering (T^2 behavior) dominates; the coefficient $A = 6(1)*10^{-5}$ mΩ.cm.K², combined with an estimate of the Sommerfield coefficient Y from the low temperature specific heat ($Y = 20.8(3)$ mJ.K⁻².mol⁻¹, see Fig. 6), gives as Kadowaki-Woods ratio (A/Y^2) of $0.13 (2)*10^{-2}$ $\mu\Omega\text{.cm}\cdot\text{mol}^2\cdot\text{K}^2\cdot\text{mJ}^{-2}$, which is close to that of hexagonal layered $\text{Na}_{0.7}\text{CoO}_2$ [38,39]. This indicates that, despite all expectations from the structure and elements involved, that the behavior is that of an uncorrelated metal. The Wilson ratio [calculations in SI] is $\sim 7.7 - 5.2$ similar to strongly correlated layered cobalt oxide [$\text{BiBa}_{0.66}\text{K}_{0.36}\text{O}_2\text{CoO}_2$] which may indicate some magnetic interaction relative to the conduction electrons [40].

E. Electronic Structure

We explore the band structures of the synthesized kagomé compounds to understand the correlation of the physical properties with the electronic structure. We computed the electronic band structures of MgCo_6Ge_6 , YCr_6Ge_6 and LuFe_6Ge_6 (Fig 7a, b, c). YCr_6Ge_6 has been claimed to be a possible candidate for kagomé metal with in-plane resistivity twice as large as the interplane resistivity. [23]. The unusual magnetic anisotropy was attributed to the presence of nearly flat bands slightly below Fermi level near the Γ point toward the K and M points, which corresponds to the direction perpendicular to the z axis in real space. In addition to this, a dispersive band has been observed from Γ to A , which corresponds to the direction along the z axis in real space (Fig 7a) [23]. Recent reports show the direct observation of the flat band associated with the d_z^2 orbital of the Cr atoms by angle-resolved photoemission spectroscopy (ARPES) [24]. We observed similar partially flat bands in LuFe_6Ge_6 running from M to Γ and from Γ to A perpendicular and parallel to z axis respectively (Fig. 7b). The dispersive band running from L to A is also found to be present in LuFe_6Ge_6 just above the Fermi level, making it a potential host for interesting physical properties. The major difference in the character of these two bands seems to be the orbital contribution, from density of states calculations the flat bands in LuFe_6Ge_6 seem to be associated with in plane $d_{x^2-y^2}$ orbitals instead of d_{z^2} . One interesting feature of these compounds is that the flat bands are dominated by the $3d$ orbitals of the

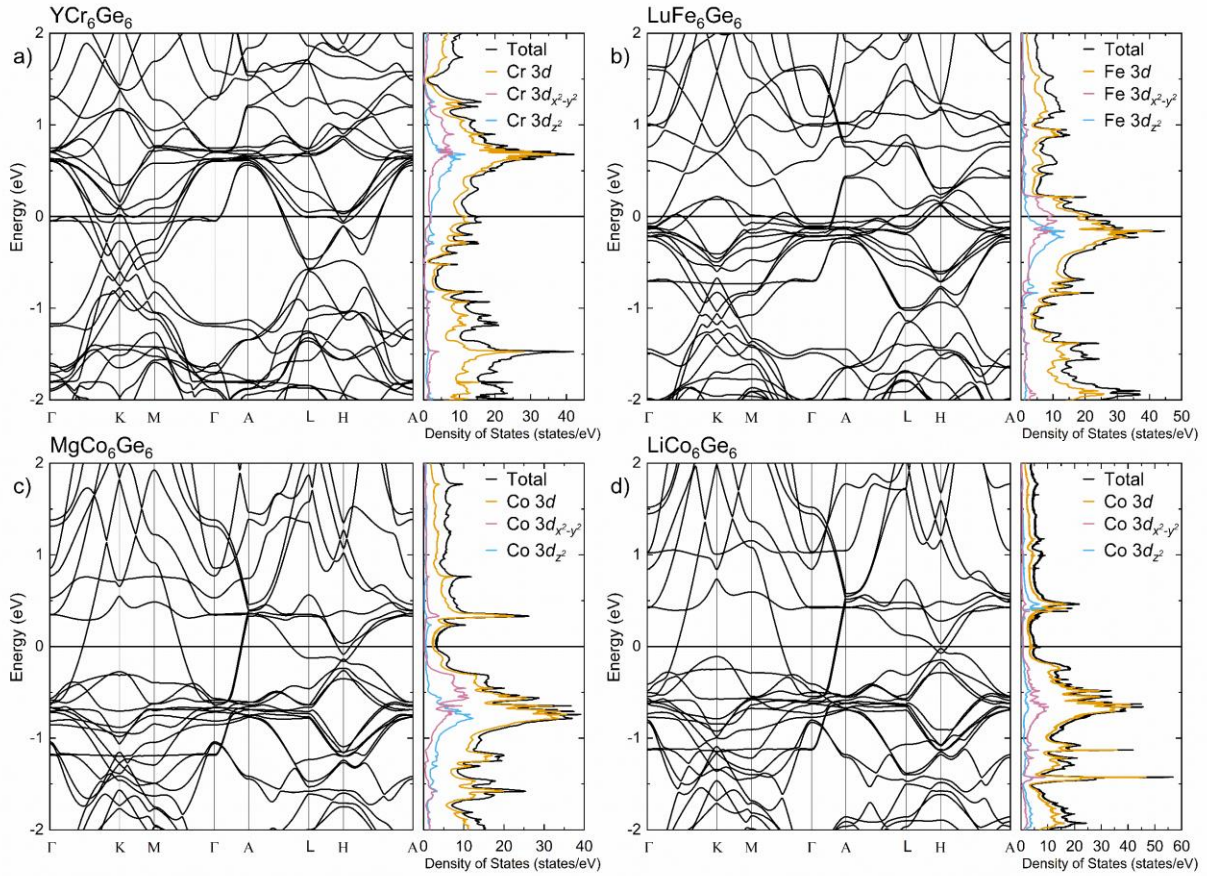


Figure 7. a) Band structure of YCr_6Ge_6 showing the presence of linearly dispersed flat bands below Fermi level near the Γ point toward the K and M points in addition to a dispersive band in the Γ - A direction. b) Similar flat bands observed in LuFe_6Ge_6 below the Fermi level in the M - Γ and Γ - A directions along with a Dirac dispersion from L - A just above the Fermi level. c) Electronic band structure calculations of MgCo_6Ge_6 in $P6/mmm$ which shows a Dirac-type dispersion running from the points L to H just below the Fermi level. d) Hole doping of the system to LiCo_6Ge_6 moves the band crossing near the Fermi level.

transition metals (Cr and Fe). No such flat bands near the Fermi level were observed in MgCo_6Ge_6 , explaining the normal metallic resistivity we observe. A Dirac-type dispersion below the Fermi level relating to the direction perpendicular to z -axis in real space from the L to H points was observed in the band structure of MgCo_6Ge_6 (Fig 7c). The partial disorder in the Mg and Ge3 atoms could not be accounted for in the band structure calculations. However, the density of states calculation show that the bands near the Fermi level are not influenced by these atoms, making it likely that the disorder has little effect on the electronic structure near the Fermi level. DFT calculations show that hole doping of the MgCo_6Ge_6 system is expected to further move the band crossing near the Fermi level (Fig 7d, See SI Fig S1 for overlapping MgCo_6Ge_6 and LiCo_6Ge_6 band structure plots). ARPES combined with transport measurements will be helpful to shed more light on

the role of the experimental band structures of these hexagonal lattice systems. Thus, obtaining large single crystals of these systems becomes crucial.

IV. CONCLUSIONS

Large single crystals of MgCo_6Ge_6 ($P6/mmm$) were obtained by laser heated Bridgman growth technique helping to overcome the vaporization of Mg at melting temperatures of the compound. SXRD data was modelled to reveal partial displacive disorder along c axis. Fits to the heat capacity data show the presence of low-lying Einstein mode corresponding to the disorder in the structure. The absence of disorder in the single crystal structures of YCr_6Ge_6 and LuFe_6Ge_6 can be ascribed to the increased coupling between the M and the Ge atoms with decrease in size of the M atom as interpreted from the specific

heat measurements. Also, the small ionic radius of Mg atom facilitates the relaxation of the Ge3-Ge3 bonds and leads to the disorder. Direction dependent low temperature ($T \sim 20$ K) magnetic susceptibility measurements on a single crystal of MgCo_6Ge_6 show anisotropy in the system similar to LuFe_6Ge_6 and YCr_6Ge_6 . The resistivity measurements show metallic behavior lacking strong electronic correlations agreeing with the electronic band structure calculations of MgCo_6Ge_6 which do not show partially flat bands near the Fermi level as observed in the case of LuFe_6Ge_6 and YCr_6Ge_6 . While the Kadowaki-Woods ratio is similar to hexagonal layered $\text{Na}_{0.7}\text{CoO}_2$, the strongly enhanced value of Wilson ratio indicates large magnetic response with respect to the number of electrons. The MgCo_6Ge_6 band structure shows a Dirac type dispersion below the Fermi level which can potentially be moved further near the Fermi level by hole doping. However, angle dependent transport measurement along with ARPES on these systems is necessary to delve deeper into the correlation of electronic structure and physical properties of these materials.

ACKNOWLEDGEMENTS

This work was supported by the David and Lucile Packard Foundation. HKV, VJS, and TTT acknowledge support of the Institute for Quantum Matter, an Energy Frontier Research Center funded by the United States Department of Energy, Office of Science, Office of Basic Energy Sciences, under Award DE-SC0019331. MKS, LAP, TB, and WAP acknowledge support of the Platform for the Accelerated Realization, Analysis, and Discovery of Interface Materials (DMR-1539918), a National Science Foundation Materials Innovation Platform. ZW, IJ and MC acknowledge support of Whiting School of Engineering, the Johns Hopkins University, and the NSF (NSF DMR-1804320). CW acknowledges the support of Hopkins Extreme Materials Institute (HEMI). Access to the Bruker 1172 instrument was also possible via the Hopkins Extreme Materials Institute (HEMI). MKS would like to thank Dr. Chris M. Pasco for the helpful discussions regarding SXRD.

References

1. J. Kübler, C. Felser, *Europhys. Lett.* **108**, 67001 (2014).
2. E. Tang, J. W. Mei, X.G. Wen, *Phys. Rev. Lett.* **106**, 236802 (2011).
3. G. Liu, P. Zhang, Z. Wang, S. S. Li, *Phys. Rev. B* **79**, 035323 (2009).
4. J. X. Yin, S. S. Zhang, G. Chang, Q. Wang2, S. S. Tsirkin, Z. Guguchia, B. Lian, H. Zhou, K. Jiang, I. Belopolski, N. Shumiya, D. Multer, M. Litskevich, T. A. Cochran, H. Lin, Z. Wang, T. Neupert, S. Jia, H. Lei, M. Z. Hasan, *Nature Physics* **15**, 443–448 (2019).
5. A. Bolens, N. Nagaosa, *Phys. Rev. B* **99**, 165141 (2019).
6. M. Kang, S. Fang, L. Ye, H. C. Po, J. Denlinger, C. Jozwiak, A. Bostwick, E. Rotenberg, E. Kaxiras, J. G. Checkelsky, R. Comin, *Nature Communications* **11**, 4004 (2020).
7. Z. Li, J. Zhuang, L. Wang, H. Feng, Q. Gao, X. Xu, W. Hao, X. Wang, C. Zhang, K. Wu, S.X. Dou, L. Chen, Z. Hu, Y. Du, *Science Advances* **16**, 4511 (2018).
8. H. M. Guo, M. Franz, *Phys. Rev. B* **80**, 113102 (2009).
9. I.I. Mazin, H. O. Jeschke, F. Lechermann, H. Lee, M. Fink, R. Thomale, R. Valenti, *Nat. Commun.* **5**, 4261 (2014).
10. L. Ye, M. Kang, J. Liu, F. von Cube, C. R. Wicker, T. Suzuki, C. Jozwiak, A. Bostwick, E. Rotenberg, D. C. Bell, L. Fu L, R. Comin, J. G. Checkelsky, *Nature* **555**, 638–642 (2018).
11. T. Kida, L.A. Fenner, A.A. Dee, I. Terasaki, M. Hagiwara, A.S. Wills, *J. Phys: Condens. Matter* **23**, 112205(6) (2011).
12. L.A. Fenner, A.A. Dee, A.S. Wills, *J. Phys: Condens. Matter* **21**, 452202(7) (2009).
13. S. I. Simak, U. Häußermann, I. A. Abrikosov, O. Eriksson, J. M. Wills, S. Lidin, and B. Johansson, *Phys. Rev. Lett.* **79**, 1333 (1997).
14. E. Liu, Y. Sun, N. Kumar, L. Muechler, A. Sun, L. Jiao, S. Y. Yang, D. Liu, A. Liang, Q. Xu, J. Kroder, V. Süß, H. Borrman, C. ShekhaR, Z. Wang, C. Xi, W. Wang, W. Schnelle, S. Wirth, Y. Chen, S. T. B. Goennenwein, C. Felser, *Nature Physics* **14**, 1125–1131 (2018).
15. Q. Wang, Y. Xu, R. Lou, Z. Liu, M. Li, Y. Huang, D. Shen, H. Weng, S. Wang H. Lei, *Nat Commun.* **9**, 3681 (2018).
16. T. Kubodera, H. Okabe, Y. Kamihara, M. Matoba, *Phys. B* **378–380**, 1142–1143 (2006).
17. J. Yin, W. Ma, T. A. Cochran, X. Xu, S. S. Zhang, H. Tien, N. Shumiya, G. Cheng, K. Jiang, B. Lian, Z. Song, G. Chang, I. Belopolski, D. Multer, M. Litskevich, Z. Cheng, X. Yang, B. Swidler, H. Zhou, H. Lin, T. Neupert, Z. Wang, N. Yao, T. Chang, S. Jia, M. Zahid Hasan, *Nature* **583**, 533-536 (2020).

18. S.-Y. Yang, Y. Wang, B.R. Ortiz, D. Liu, J. Gayles, E. Derunova, R. Gonzalez-Hernandez, L. Smejkal, Y. Chen, S.S.P. Parkin, S.D. Wilson, E.S. Toberer, T.M. McQueen, M.N. Ali, *Science Advances* **6**, eabb6003 (2020).
19. B.R. Ortiz, L.C. Gomes, J.R. Morey, M.J. Winiarski, M. Bordelon, J.S. Mangum, I.W.H. Oswald, J.A. Rodriguez-Rivera, J.R. Neilson, S.D. Wilson, E. Ertekin, T.M. McQueen, E.S. Toberer, *Phys. Rev. Mater.* **3**, 094407 (2019).
20. G. Venturini, R. Welter, B. Malaman, *J. Alloys Compd.* **185**, 99 (1992).
21. J.M. Cadogan, D.H. Ryan, *J. Alloys Compd.* **326**, 166 (2001).
22. V.W. Buchholz, H.U. Schuster, *Z. Anorg. Allg. Chem.* **482**, 40 (1981).
23. P. Schobinger-Papamantellos, J. Rodrguez-Carvajal, K. H. J. Buschow, *Journal of Alloys and Compounds* **255**, 67-73 (1997).
24. Y. Ishii, H. Harima, Y. Okamoto, J. Yamaura, Z. Hiroi, *J. Phys. Soc. Jpn.* **82**, 023705 (2013).
25. P. C. Canfield, Z. Fisk, *Phil. Mag. B*, **65**, 1117 (1992).
26. P. C. Canfield and I. R. Fisher, *J. Cryst. Growth* **225**(2), 155-161 (2001).
27. W. Du, D. Xu, H. Zhang, X. Wang, G. Zhang, X. Hou, H. Liu, Y. Wang, *Journal of Crystal Growth* **268**, 123–127 (2004).
28. M. Straker, A. Chauhan, M. Sinha, W.A. Phelan, M.V.S. Chandrashekhar, K.J. Hemkar, C. Marvel, M. Spencer, *Journal of Crystal Growth*, **543**, 125700 (2020).
29. K. Momma, F. Izumi, *J. Appl. Crystallogr.* **44**, 1272–1276 (2011).
30. R. D. Hanna, R. A. Ketcham, *Chemie der Erde* **77**, 547–572, (2017).
31. G. Venturini, H. Ihou-Mouko, C. Lefevre, S. Lidin, B. Malaman, T. Mazet, J. Tobola, A. Verniere, *Chem. Met. Alloys* **1**, 24-33 (2008).
32. P. Schobinger-Papamantellos, J. Rodrguez-Carvajal, G. Andre, K. H. J. Buschow, *Journal of Magnetism and Magnetic Materials* **150-3**, 311-322 (1995).
33. D. Johrendt, H. Hosono, R.D. Hoffmann, R. Pottgen, J. Rouxel, *J. Solid State Chem.* **130**, 254-265 (1997).
34. M. Sinha, T.J. Pearson, T.R. Reeder, H.K. Vivanco, D.E. Freedman, W.A. Phelan, T.M. McQueen, *Phys. Rev. Materials*, **3**, 125002 (2019).
35. B. C. Melot, R. Tackett, J. O'Brien, A. L. Hector, G. Lawes, R. Seshadri, A. P. Ramirez, *Phys. Rev. B* **79**, 224111 (2009).
36. A. Tari, Imperial College Press, London (2003).
37. A. P. Ramirez, G. R. Kowach, *Phys. Rev. Lett.* **80**, 4903 (1998).
38. S. Y. Li, L. Taillefer, D. G. Hawthorn, M. A. Tanatar, J. Paglione, M. Sutherland, R. W. Hill, C. H. Wang, and X.H. Chen, *Phys. Rev. Lett.* **93**, 056401(2004).
39. A. Jacko, J. Fjærstad, B. Powell, *Nature Phys* **5**, 422–425 (2009).
40. P. Limelette, H. Muguerra, S. Hebert, *Phys. Rev. B* **82**, 035123 (2010).